Opto-Electronic
Science

Reconfigurable origami chiral response for holographic imaging and information encryption

Zhibiao Zhu, Yongfeng Li*, Jiafu Wang*, Ze Qin, Lixin Jiang, Yang Chen, Shaobo Qu

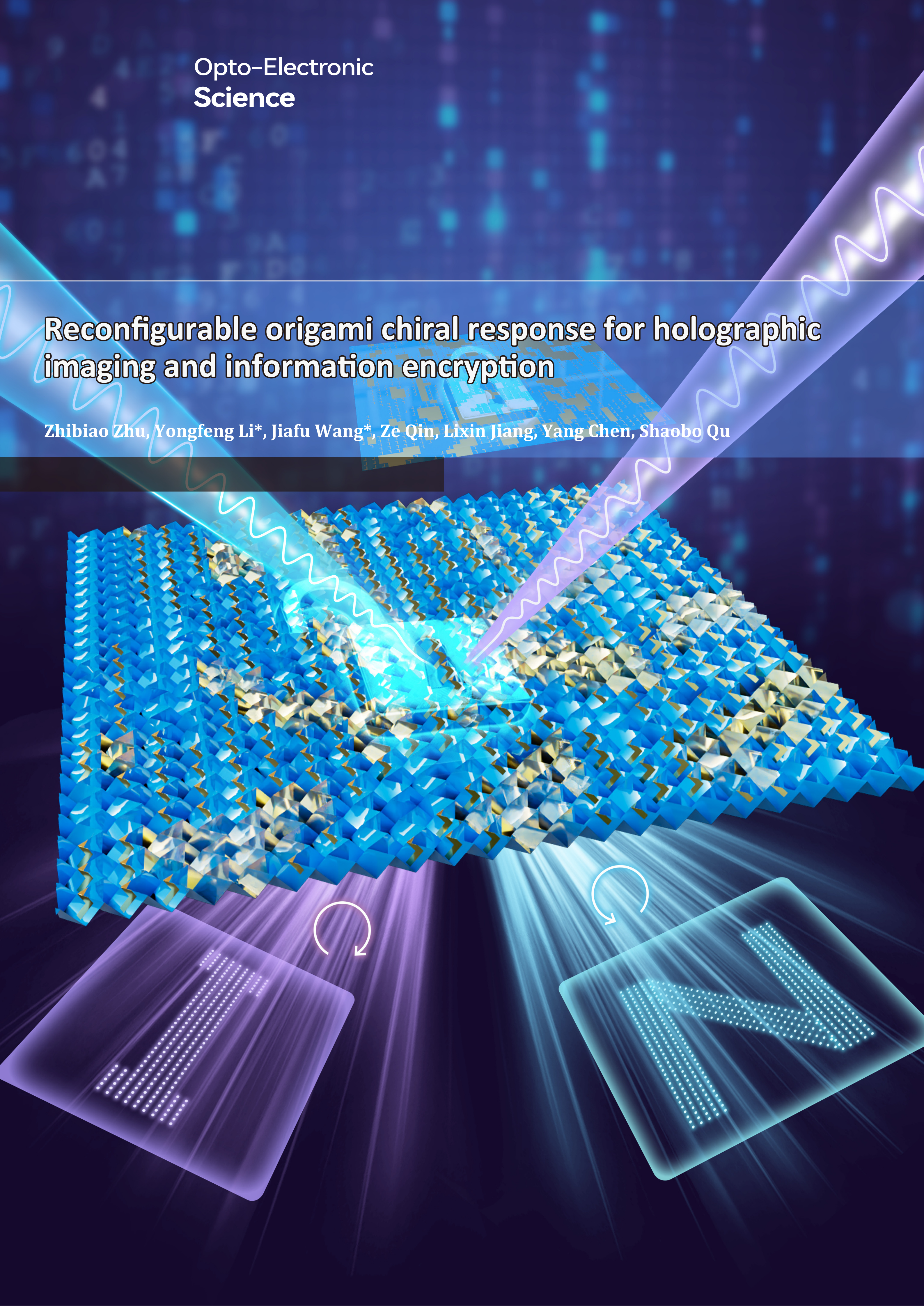

Opto-Electronic
Science

CN 51−1800/O4 ISSN 2097−0382 (Print) ISSN 2097−4000 (Online)

Reconfigurable origami chiral response for holographic imaging and information encryption

Zhibiao Zhu, Yongfeng Li, Jiafu Wang, Ze Qin, Lixin Jiang, Yang Chen and Shaobo Qu

Citation: Zhu ZB, Li YF, Wang JF, et al. Reconfigurable origami chiral response for holographic imaging and information encryption. *Opto-Electron Sci* **4**, 240026 (2025).

Received: 28 September 2024; Accepted: 19 November 2024; Published online: 21 February 2025

Related articles

Multi-dimensional multiplexing optical secret sharing framework with cascaded liquid crystal holograms
Keyao Li, Yiming Wang, Dapu Pi, Baoli Li, Haitao Luan, Xinyuan Fang, Peng Chen, Yanqing Lu, Min Gu
Opto-Electronic Advances 2024 **7**, 230121 doi: 10.29026/oea.2024.230121

Racemic dielectric metasurfaces for arbitrary terahertz polarization rotation and wavefront manipulation
Jie Li, Xueguang Lu, Hui Li, Chunyu Song, Qi Tan, Yu He, Jingyu Liu, Li Luo, Tingting Tang, Tingting Liu, Hang Xu, Shuyuan Xiao, Wanxia Huang, Yun Shen, Yan Zhang, Yating Zhang, Jianquan Yao
Opto-Electronic Advances 2024 **7**, 240075 doi: 10.29026/oea.2024.240075

Liquid crystal-integrated metasurfaces for an active photonic platform
Dohyun Kang, Hyeonsu Heo, Younghwan Yang, Junhwa Seong, Hongyoon Kim, Joohoon Kim, Junsuk Rho
Opto-Electronic Advances 2024 **7**, 230216 doi: 10.29026/oea.2024.230216

Generation of structured light beams with polarization variation along arbitrary spatial trajectories using tri-layer metasurfaces
Tong Nan, Huan Zhao, Jinying Guo, Xinke Wang, Hao Tian, Yan Zhang
Opto-Electronic Science 2024 **3**, 230052 doi: 10.29026/oes.2024.230052

Opto-Electronic Science

Article

April 2025, Vol. 4, No. 4

DOI: 10.29026/oes.2025.240026 CSTR: 32246.14.oes.2025.240026

Reconfigurable origami chiral response for holographic imaging and information encryption

Zhibiao Zhu, Yongfeng Li*, Jiafu Wang*, Ze Qin, Lixin Jiang, Yang Chen and Shaobo Qu

With the rapid development of holographic technology, metasurface-based holographic communication schemes have demonstrated immense potential for electromagnetic (EM) multifunctionality. However, traditional passive metasurfaces are severely limited by their lack of reconfigurability, hindering the realization of versatile holographic applications. Origami, an art form that mechanically induces spatial deformations, serves as a platform for multifunctional devices and has garnered significant attention in optics, physics, and materials science. The Miura-ori folding paradigm, characterized by its continuous reconfigurability in folded states, remains unexplored in the context of holographic imaging. Herein, we integrate the principles of Rosenfeld with L- and D-metal chiral enantiomers on a Miura-ori surface to tailor the aperture distribution. Leveraging the continuously tunable nature of the Miura-ori's folded states, the chiral response of the metallic structures varies across different folding configurations, enabling distinct EM holographic imaging functionalities. In the planar state, holographic encryption is achieved. Under specific folding conditions and driven by spin circularly polarized (CP) waves at a particular frequency, multiplexed holographic images can be reconstructed on designated focal planes with CP selectivity. Notably, the fabricated origami metasurface exhibits a large negative Poisson ratio, facilitating portability and deployment and offering novel avenues for spin-selective systems, camouflage, and information encryption.

Keywords: origami; reconfigurable; chiral response; holographic imaging; information encryption

Zhu ZB, Li YF, Wang JF et al. Reconfigurable origami chiral response for holographic imaging and information encryption. *Opto-Electron Sci* **4**, 240026 (2025).

Introduction

Metamaterials, composed of artificially designed subwavelength units, offer extensive design freedoms across multiple dimensions, including frequency, amplitude, phase, and polarization. This versatility has enabled the revelation of various exotic physical phenomena within the realm of electromagnetic (EM) metamaterials, such as anomalous reflection/refraction[1,2], generation of vortex beams[3–5], perfect absorbers[6], and meta-holograms[7–12]. Among these applications, metasurface-driven information encryption devices have garnered significant attention[13–16]. By encoding independent phase profiles across different frequency bands and polarization states, these devices achieve non-reconfigurable information encryption within a single structure[17]. As signal processing and imaging systems place greater demands on the dynamic manipulation of EM waves, active and tunable metasurfaces have been proposed and utilized, providing a flexible platform for realizing diverse applications and devices[18]. Current approaches to dynamic control include

Shaanxi Key Laboratory of Artificially-Structured Functional Materials and Devices, Air Force Engineering University, Xi'an 710051, China.

Received: 28 September 2024; Accepted: 19 November 2024; Published online: 21 February 2025

integrating field-programmable gate arrays (FPGAs) into dynamic metasurfaces or utilizing graphene and phase-change materials to modulate the amplitude of EM waves[13−22]. However, these dynamic control methods possess certain drawbacks, such as high costs, bulky structures, and significant power consumption. Particularly for active programmable metasurfaces, the complexities of feed networks and insertion losses must also be taken into account.

The introduction of origami art into metasurface design has emerged as a promising alternative for designing reconfigurable metasurfaces. By leveraging the principles of origami, metasurfaces can be endowed with the capability to transform their EM properties through simple mechanical manipulations, offering a cost-effective, lightweight, and efficient solution to the challenges faced by traditional dynamic metasurface technologies. Origami is an art form that transforms two-dimensional (2D) paper into three-dimensional (3D) structures. It originated in China during the 1st century AD, coinciding with the invention of papermaking. Subsequently, Japan developed origami into more intricate designs, such as the renowned paper crane. In recent years, origami art has begun to make significant strides in fields such as engineering, materials science, and physics, encompassing applications in aerospace structures[23,24], metamaterials[25−29], biomedical devices[30], reconfigurable electronics[31], and architecture[32]. Furthermore, in EMs, numerous scientists have harnessed origami's unique structural and mechanically reconfigurable characteristics to achieve various functionalities. Examples include chiral responses[33], EM beam deflection[34], broadband absorption[35], and reconfigurable polarization converters[36]. Compared to complex, bulky, and costly active multifunctional metasurfaces, origami metasurfaces require only a single sheet of lightweight paper, eliminating the need for energy-intensive external stimuli such as voltage.

Origami/kirigami metasurfaces offer a novel approach to manipulating EM waves by mechanically transforming their structures, thereby altering their EM properties and introducing a new degree of freedom for EM wave manipulation[37−40]. In particular, the chiral effects emerging from transforming subwavelength planar arrays into 3D configurations serve as an auxiliary dimension for manipulating EM waves or generating holograms[41−44]. Through structural deformation, origami metasurfaces rearrange the spatial positions of loaded metallic structures, leading to significant chiral responses[33,45]. Furthermore, the mechanical tunability of origami metasurfaces enables the reconfigurability of the generated chiral responses. However, the currently designed reconfigurable chiral origami metasurfaces exhibit relatively monotonic functionalities. The aforementioned origami metasurfaces primarily achieve chiral responses at specific operating frequencies, with limited further exploration into regulating EM functionalities. The Miura-ori origami metasurface, with its bianisotropic structure, is an ideal platform for realizing chiral responses. Compared to other types of origami, Miura-ori folding exhibits continuous adjustability and exceptional mechanical properties, which facilitate the stability of structural performance during both folding and unfolding processes[25,28]. Nevertheless, the work in ref.[33] failed to achieve wavefront manipulation or further holographic imaging at the chiral response frequency, limiting its applications.

Addressing the challenges mentioned above, we propose adopting the Miura-ori origami form to transform 2D metallic structures into 3D configurations through mechanical manipulation. The high degree of asymmetry inherent in the 3D metallic structures gives rise to chiral responses, manifested as the differential transmission of orthogonal circularly polarized (CP) waves. Furthermore, we leverage the structural symmetry to design enantiomeric forms of the folded chiral structures. As a proof-of-concept demonstration, we printed arranged metallic structures on a polyimide film and reconstructed spin-decoupled holographic images under different folded states through origami deformation. Both numerical simulations and experimental verifications are conducted in the microwave frequency range. Under appropriate folded states, our proposed origami metasurface reconstructs pre-designed letters "N" [upon left-handed circularly polarized (LCP) incidence] and "I" [upon right-handed circularly polarized (RCP) incidence] on the corresponding focal planes. When the origami metasurface is in its planar state, the absence of chiral responses within the metallic structures results in the disappearance of the corresponding holographic images, rendering the retrieval of valuable information impossible. Given the flexible deformation and reconfiguration capabilities of the Miura-ori origami metasurface, the proposed design holds potential applications in EM camouflage and information encryption within communication and imaging systems.

Principle and unit cell design

The concept of the Miura-ori metasurface for holographic image generation and information encryption is illustrated in Fig. 1. When the origami metasurface is in its folded state, the structure encodes image information for two independent channels. Under the induction of LCP and RCP, two distinct holographic images can be observed on the focused planes corresponding to the same frequency. Conversely, when the origami metasurface is in its planar state, the symmetry of the metallic enantiomeric structures is only slightly perturbed, failing to generate a significant chiral response. Consequently, the encoding sequences of both channels are disrupted, rendering it impossible for observers to retrieve useful information. Therefore, this origami form, serving as a disguised device for information encryption, holds promising applications in fields such as information security and target jamming.

To realize holographic imaging with independent encoding for LCP and RCP, copper patterns are printed on an ultra-thin polyimide substrate (with a relative permittivity of 3.4, a loss tangent of 0.005, and a thickness of 50 μm) using printed circuit board (PCB) printing technology. L- and D-enantiomers are designed to exhibit opposite chiral responses. These enantiomers enable the distinction between LCP and RCP. Figure 2(a) and 2(b) illustrate the planar state of the origami structure, where the L-shaped metallic structure consists of two metallic strips. Additionally, to demonstrate how the origami deforms, creases representing mountain and valley folds are marked on the surface of the planar substrate. Notably, the unit cell of the Miura-ori is redefined, and the simulation settings refer to our previous work[33]. Individually, each enantiomer lacks mirror symmetry within its structure. However, the L- and D-enantiomers are mirror images of each other about the *xOz* plane, resulting in complementary properties. Figure 2(c) presents the simulated transmission spectra and circular dichroism (CD) values as a function of frequency for the enantiomers in their planar state. The metallic structure in the planar state cannot distinguish between the two spin states of the incident waves, leading to identical transmission simulation curves under LCP and RCP illuminations. Consequently, the CD value remains nearly zero across the operational frequency band in this state. The enantiomers are configured into 3D structures utilizing the Miura-ori origami geometry to break the spin degeneracy. When the in-plane symmetry of the metallic structure is disrupted, and asymmetry along the *z*-axis is introduced, chiral resonances occur. This deformation enhances the transmission for one spin state while blocking the opposite. As shown in Fig. 2(d) and 2(e), when the origami is folded, the metallic structures attached to the surface naturally transform into 3D configurations. The folding angle, denoted as θ, relates to the periodicity of the origami structure in the *x* and *y* directions, which

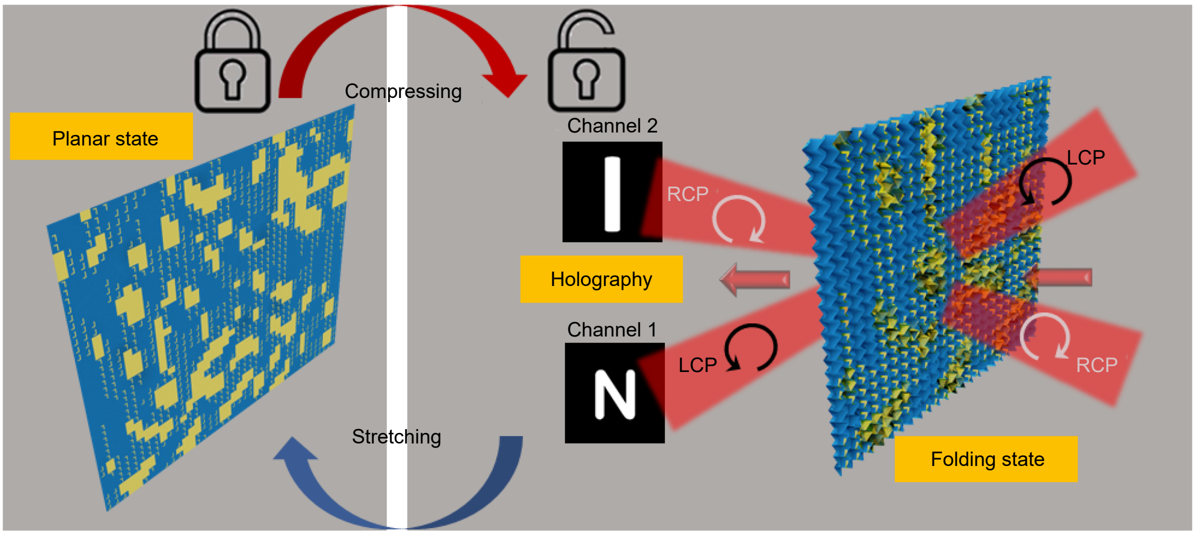

Fig. 1 | Schematic illustration of a dynamic multifunctional metasurface based on Miura-ori. The reconfigurable origami metasurface enables the display or concealment of image information for dynamic display and encryption. In the planar state, the chiral response of the unit cells remains inactive, resulting in scrambled encoding sequences across both channels, which prevents the normal display of images. Upon folding the origami metasurface, the incident CP light (including both RCP and LCP) decodes two far-field holographic images (Channel 1 and Channel 2).

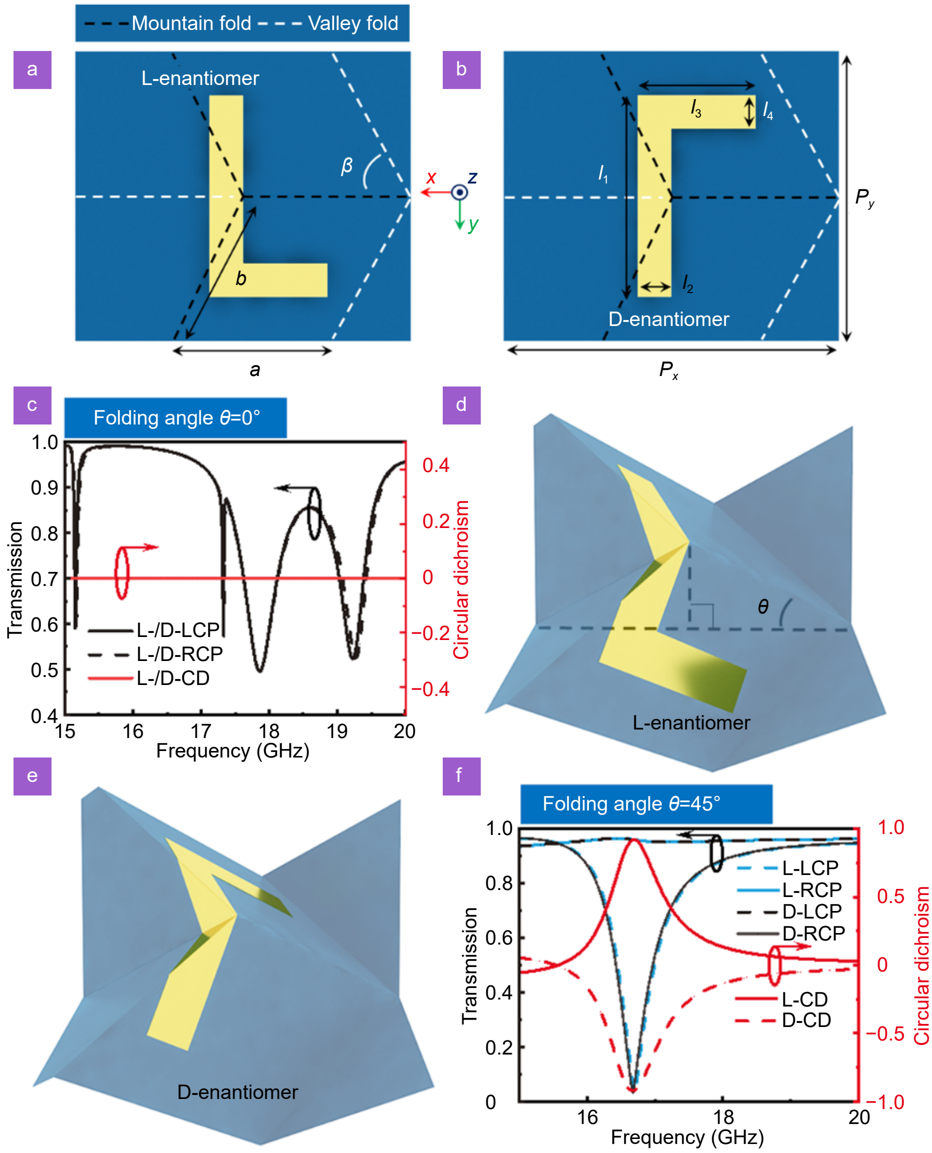

Fig. 2 | Transmission characteristics of the Miura-ori unit cell structure. (**a**, **b**) The L- and D-enantiomer unit cell structures are in the planar state. a=b=10 mm, l_1=12 mm, l_2=l_4=2 mm, l_3=7 mm, β=60°. The L- and D-enantiomers have a periodicity of P_x in the x-direction and P_y in the y-direction. Note that P_x and P_y are dynamically changing as the folded state varies. (**c**) Transmission magnitude and CD values as a function of frequency when the L- and D-enantiomer unit cell structures are in the planar state. (**d**, **e**) The L- and D-enantiomer unit cell structures in the folded state. θ represents the unique degree of freedom describing the folded state of the Miura-ori. (**f**) Transmission magnitude and CD values as a function of frequency when the L- and D-enantiomer unit cell structures are in the folded state (θ=45°).

can be mathematically expressed as follows:

$$\begin{cases} P_x = 2b(\sin\delta\cos\beta + \cos\delta\cos\theta\sin\beta) \\ P_y = 2a\cos\delta \end{cases}, \qquad (1)$$

where, $\delta = \arctan\left[\dfrac{1}{\tan\beta\cos\theta}\right]$. In this context, the in-plane and rotational symmetry of the metallic structure are completely broken, leading to a strong chiral response. To quantitatively analyze the chirality of the metasurface, the CD value is defined as CD=$|T_{\mathrm{LCP}}|-|T_{\mathrm{RCP}}|$, where T_{LCP} and T_{RCP} represent the transmission intensities of LCP and RCP, respectively. T_{RCP} is given by $|t_{\mathrm{RR}}|^2+|t_{\mathrm{LR}}|^2$, and T_{LCP} is given by $|t_{\mathrm{RL}}|^2+|t_{\mathrm{LL}}|^2$. Where $t_{\mathrm{RL(LR)}}$ is the cross-polarized transmission coefficient, $t_{\mathrm{RR(LL)}}$ is the co-polarized transmission coefficient. When the folding angle θ=45°, the simulated transmission spectra of the folded L- and D-enantiomers are shown in Fig. 2(f).

Distinct differences can be observed in the transmission spectra of LCP and RCP. For the L-enantiomer, the transmission of RCP is suppressed ($|t_{\mathrm{RR}}| = 0.13$) at the operating frequency $f = 16.7$ GHz, while LCP is nearly transparent ($|t_{\mathrm{LL}}| = 0.96$). The chiral response characteristics of the D- and L-enantiomers are complementary. Figure 2(f) displays the corresponding CD curves of the folded L- and D-enantiomers. Notably, two prominent CD resonances with opposite intensities appear in the CD spectrum. The enantiomeric origami unit cells provide the desired pronounced CD in opposite manners. The CD magnitudes of the L- and D-enantiomers at $f = 16.7$ GHz are ±0.92, respectively. Furthermore, the cross-polarized transmission magnitudes of LCP and RCP ($|t_{\mathrm{LR}}|$ and $|t_{\mathrm{RL}}|$), are similarly suppressed (Fig. 3(a)). This suggests that the folded unit cells significantly break the spin degeneracy of the incident waves, enabling efficient spin-selective transmission. By carefully arranging the aperture distribution, significant potential is provided for realizing amplitude-based meta-holograms. To reconstruct the desired holographic image, it is also necessary to employ unit cells that achieve high/low transmission efficiencies for both LCP and RCP simultaneously as auxiliaries. Here, unit cells in the form of metal patch overlays and those composed solely of the substrate are suitable for fulfilling this requirement (Fig. 3(b)). In this design, metal-coated and substrate-only meta-atoms are employed to meet these requirements. Notably, the distribution of creases on the surface of the proposed auxiliary units aligns with that presented in Fig. 2. The corresponding transmission spectra are illustrated in Fig. 3(c). Evidently, the proposed unit cells successfully meet the requirements within the 15–20 GHz frequency range, encompassing the operating frequency of 16.7 GHz. To realize the predefined holographic encryption functionality, metal-coated meta-atoms, L-enantiomers, D-enantiomers, and substrate-only meta-atoms are individually applied to fit the binary amplitude operations for the four combined pixels (0, 0), (0, 1), (1, 0), and (1, 1).

To delve into the physical mechanisms underlying the chiral response elicited by L- and D-enantiomers, the surface current distributions of planar/folded unit cells at 16.7 GHz are monitored under the illumination of LCP and RCP. According to the Rosenfeld criterion, the chiral response is inherently triggered by the cross-coupling between the electric and magnetic fields, with the necessary condition being $\sum \boldsymbol{P}\cdot\boldsymbol{M}\neq 0$, where $\boldsymbol{P}$ and $\boldsymbol{M}$ represent the electric and magnetic dipoles, respectively. Upon transitioning the Miura-ori metasurface into its 3D configuration, it comprises four facets. In this state, the surface currents induce the generation of electric and mag-

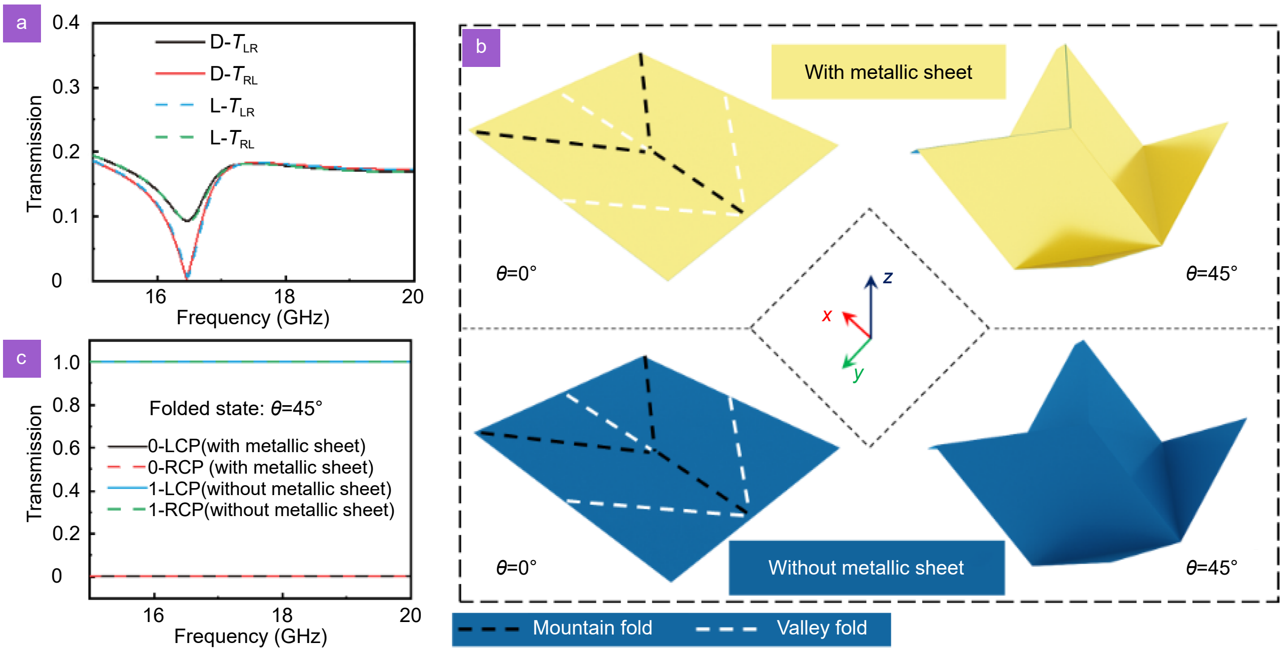

Fig. 3 | (**a**) Cross-polarization transmission coefficients for the folded L- and D-enantiomer unit cells. t_{RL} represents the cross-polarization coefficient when illuminated by LCP. t_{LR} denotes the cross-polarization coefficient for RCP incidence (θ=45°). (**b**) Unit cells that implement LCP and RCP 0 and 1 transmission. There is a metal layer covering, to achieve 0 transmission. No metal layer covering, pure media substrate, to achieve 1 transmission. (**c**) The transmission spectra of the unit cells (θ=45°).

netic dipoles whose orientations are no longer orthogonal. Evidently, under CP incidence, an efficient cross-coupling between the electric and magnetic fields is achieved. Furthermore, the electric dipole (***P***) and magnetic dipole (***M***) can be mathematically expressed as:

$$\begin{cases} \boldsymbol{P} = \boldsymbol{P}_{\text{eff},\ x} \cdot \hat{x} + \boldsymbol{P}_{\text{eff},\ y} \cdot \hat{y} + \boldsymbol{P}_{\text{eff},\ z} \cdot \hat{z} \\ \boldsymbol{M} = \boldsymbol{M}_{\text{eff},\ x} \cdot \hat{x} + \boldsymbol{M}_{\text{eff},\ y} \cdot \hat{y} + \boldsymbol{M}_{\text{eff},\ z} \cdot \hat{z} \end{cases} . \tag{2}$$

In the given formula, $\boldsymbol{P}_{\text{eff},\ i}$ represents the effective electric field intensity with the unit vector along the direction i (where i=x, y, z), and $\boldsymbol{M}_{\text{eff},\ i}$ denotes the effective magnetic field intensity along the same direction i. Firstly, the surface current distributions of the unit cell in its planar state at the resonance frequency are compared, as illustrated in Fig. 4(a–b). In this scenario, the planar meta-atom exhibits insensitivity to different CP waves. It is observed that at 16.7 GHz, the surface current distribution splits into two oscillating directions, specifically oscillating within the short metal strips along the y-direction and the long metal strips along the x-direction. The chiral enantiomers, when in their planar state, exhibit orthogonal superposed electric and magnetic dipoles. In the planar state, the formula derivations for incident EM wave of both LCP and RCP are presented as follows:

$$\begin{cases} \text{L - enantiomer: } \sum \boldsymbol{P} \cdot \boldsymbol{M} = (-\boldsymbol{P}_2 \cdot \hat{x} + \boldsymbol{P}_1 \cdot \hat{y}) \\ \qquad \cdot (\boldsymbol{M} \cdot \hat{z}) = 0 \\ \text{D - enantiomer: } \sum \boldsymbol{P} \cdot \boldsymbol{M} = (\boldsymbol{P}_2 \cdot \hat{x} + \boldsymbol{P}_1 \cdot \hat{y}) \\ \qquad \cdot (\boldsymbol{M} \cdot \hat{z}) = 0 \end{cases} . \tag{3}$$

Consequently, the magnetic and electric dipoles excited in the planar chiral structure adhere to the rule ∑***P***·***M***=0, leading to an inconspicuous chiral response. Subsequently, the surface current distributions of the enantiomers in their folded states are investigated. Figure 4(c, d) depict the surface current distributions for L-enantiomer driven by LCP and RCP waves, respectively, at 16.7 GHz. Under RCP excitation, a pronounced resonance is clearly observed. In contrast, the surface currents induced by LCP are weak, resulting in no discernible response. Given that the chiral response characteristics of enantiomers are opposite, the surface current distribution of the D-enantiomer is precisely the inverse of that of the L-enantiomer, as shown in Fig. 4(e, f). In the 3D state, the formula derivations for both L- and D-eanatiomers are presented as follows:

$$\begin{cases} \text{L - enantiomer/RCP: } \sum \boldsymbol{P} \cdot \boldsymbol{M} = (-\boldsymbol{P}_1 \cdot \bar{a}_3 + \boldsymbol{P}_1 \cdot \bar{a}_1) \\ \cdot (\boldsymbol{M} \cdot (\bar{a}_1 \times \bar{a}_2) \cdot \hat{z}) = -\boldsymbol{M} \cdot \boldsymbol{P}_1 \cdot (\bar{a}_1 \times \bar{a}_2) \cdot \bar{a}_3 \neq 0 \\ \text{D - enantiomer/LCP: } \sum \boldsymbol{P} \cdot \boldsymbol{M} = (\boldsymbol{P}_1 \cdot \bar{a}_3 - \boldsymbol{P}_2 \cdot \bar{a}_2) \\ \cdot (\boldsymbol{M} \cdot (\bar{a}_1 \times \bar{a}_2) \cdot \hat{z}) = \boldsymbol{M} \cdot \boldsymbol{P}_1 \cdot (\bar{a}_1 \times \bar{a}_2) \cdot \bar{a}_3 \neq 0 \end{cases} . \tag{4}$$

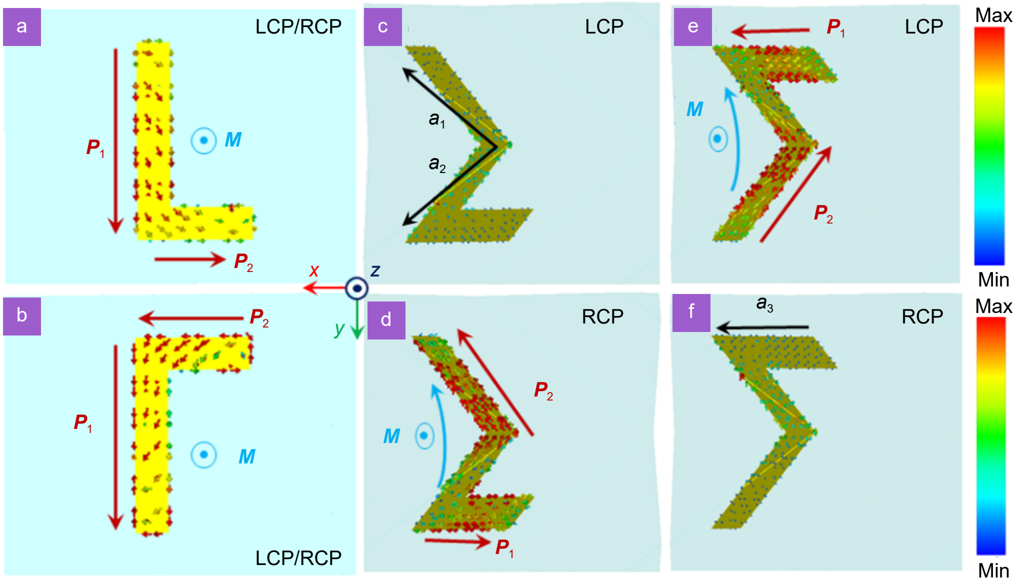

Fig. 4 | The surface current distribution of the proposed origami enantiomer, *f*=16.7 GHz. The plane state corresponding to (**a**) L-enantiomer and (**b**) D-enantiomer, the surface current distribution is the same under LCP and RCP irradiation. The surface currents corresponding to the folded L-enantiomers (θ=45°) are distributed under (**c**) LCP and (**d**) RCP irradiation. The surface currents of folded D-enantiomers (θ=45°) are distributed under (**e**) LCP and (**f**) RCP irradiation.

where $\boldsymbol{a}_i$ is the i-th edge vector of the parallelogram as illustrated in Fig. 4. Since both the electric and magnetic dipoles are distributed in a three-dimensional spatial configuration, the superposed electric and magnetic dipoles satisfy $\sum \boldsymbol{P} \cdot \boldsymbol{M} \neq 0$, triggering a strong chiral resonance. It can be observed from the equation that the derived results for the folded L and D enantiomers exhibit opposite signs, which further confirms their opposing chiral response characteristics. In summary, the aforementioned phenomena demonstrate that the folded enantiomer structure successfully fulfills the Rosenfeld criterion and breaks the degeneracy between the two spin states, leading to high transmission for one spin state and high reflection for the other.

With the assistance of origami enantiomers and auxiliary meta-atoms, binary amplitude control can be achieved within the origami aperture through rational adjustment of the folded states. To demonstrate the fundamentals of holographic imaging and encryption based on the Miura-ori folding method, a meta-hologram is designed to reconstruct the images of "N" and "I" at a distance of 20 mm from the origami aperture, and experimental validation is conducted in the microwave frequency band. As shown in Fig. 5(a), the phase responses of the four kinds of the folding unit cells are relatively consistent across the operating frequency band, providing a foundation for realizing amplitude-based holograms. The flowchart for realizing the meta-hologram is depicted in Fig. 5(b). The virtual images of "N" and "I" are independently input to meet the requirements. At the corresponding resonant frequency of 16.7 GHz, the amplitude distribution of the reconstructed holographic image is calculated using the point source method. To obtain the amplitude distribution required for reconstructing dual-channel meta-hologram, the complex amplitude profiles (E_{N} and E_{I}) of the aperture distribution are calculated using the Rayleigh-Sommerfeld diffraction theory[45]. Subsequently, based on the real parts of E_{N} and E_{I}, an amplitude hologram in 0/1 binary code for the transmission region is generated[46]:

$$\begin{cases} \mathrm{real}(E_{\mathrm{N}}(i,\ j)) > 0), \ A_{\mathrm{N}}(i,\ j) = 1; \\ \mathrm{real}(E_{\mathrm{N}}(i,\ j)) < 0), \ A_{\mathrm{N}}(i,\ j) = 0; \\ \mathrm{real}(E_{\mathrm{I}}(i,\ j)) > 0), \ A_{\mathrm{I}}(i,\ j) = 1; \\ \mathrm{real}(E_{\mathrm{I}}(i,\ j)) < 0), \ A_{\mathrm{I}}(i,\ j) = 0 \end{cases} . \tag{5}$$

In the equation, (i, j) represents the coordinates in the hologram, while A_{N} and A_{I} denote the transmission amplitudes. Here, two holograms are generated based on the signs of the real parts of the complex amplitude profiles E_{N} and E_{I}, respectively. Since the underlying principle of holography is based on the interference between the object beam and the reference beam, the real parts can represent this information. The amplitude distribution of the aperture array is encoded according to $A_{\mathrm{N}}(i, j)$ and $A_{\mathrm{I}}(i, j)$. Following the input images of "N" and "I" as indicated in the flowchart, binary combinations of pixels (0,0), (0, 1), (1, 0), (1, 1) are used to fill the corresponding positions. Here, the binary codes "0" and "1" represent lower and higher transmission intensities,

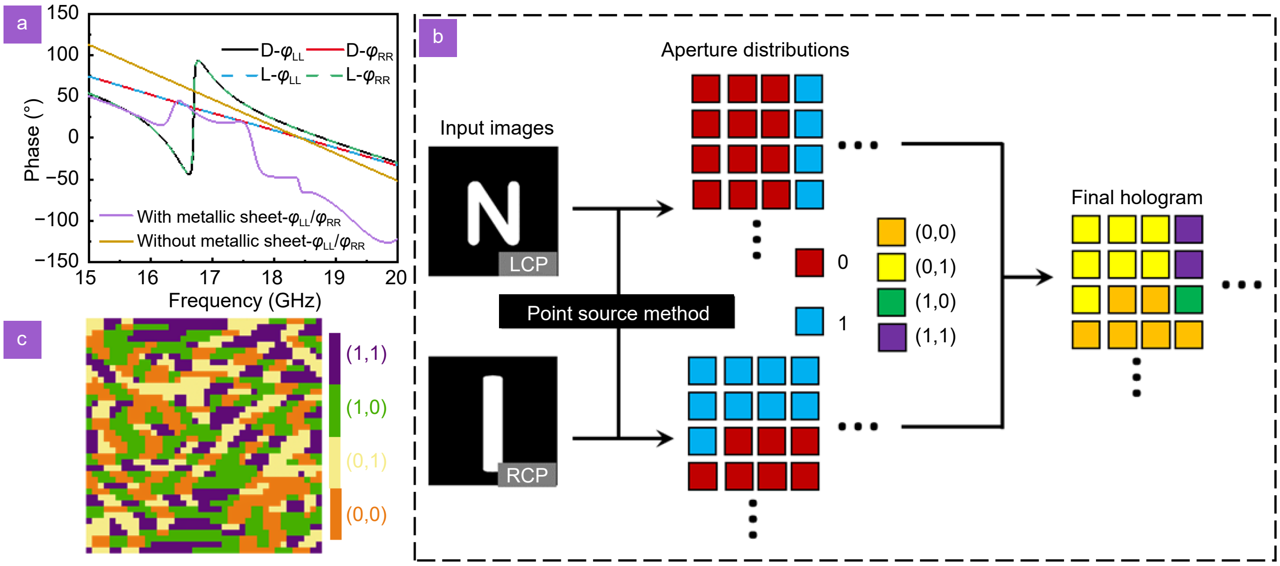

Fig. 5 | (**a**) The phase responses of the four kinds of unit cells (θ=45°). L-/D-enantiomers, with/without metallic sheets in folded states. (**b**) The flowchart for generating the required meta-hologram. (**c**) The position distribution of the four kinds of apertures which composed the origami metasurface.

respectively. Consequently, four combined pixels of (0, 0), (0, 1), (1, 0), (1, 1) are obtained, and binary amplitude manipulation is performed in the designated frequency band (Fig. 5(c)).

As a proof-of-concept, a 40 × 40 pixel prototype is fabricated, with a total size of 800 × 692.8 mm^2 in the planar state, as shown in Fig. 6(a). Additionally, when the folding angle θ = 45°, the dimensions in the x and y directions are 506 × 490 mm^2, as depicted in Fig. 6(b). Figure 6(c) presents a localized image of the folded state. We employ CNC precision milling technology to etch Miura-ori creases onto a preformed Teflon substrate (with a dielectric constant of 3 and a thickness of 0.3 mm). Upon completion of the crease etching, the origami structure can be transformed into a folded state along these creases. Subsequently, an ultra-thin polyimide film printed with metal patches is adhered to the Miura substrate. After undergoing etching by the CNC precision milling machine, the thickness of the dielectric substrate at the creases is less than that at other locations on a single panel. The design of the creases allows for considerable flexibility in the folding process. By applying mechanical stimulation, the folded state of the origami can be altered.

For verification, we conducted electric field distribution measurements in an anechoic chamber using near-field scanning techniques to characterize the pre-designed origami hologram. The origami sample is aligned horizontally with the transmitting horn antenna. Additionally, the distance between the sample and the horn antenna is set sufficiently far apart to ensure quasi-plane wave illumination on the sample surface. The scanning probe is positioned on the opposite side of the origami metasurface sample, allowing for free movement within the xOy plane (parallel to the origami metasurface). During the measurement process, the transmitter antenna and the probe are connected to two ports of the network analyzer (Fig. 6(d)), respectively. The scanning area is 506 × 490 mm^2 with a step size of 5 mm.

At the resonant frequency f=16.7 GHz of the chiral structure, both simulation and measurement results under both LCP and RCP illumination indicate that the origami metasurface achieves encryption functionality in the planar state, preventing observers from obtaining valuable information, as shown in Fig. 7(a, b) and 7(e, f). For comparison, Fig. 7(c, d) present the simulated holographic images of "N" (LCP channel) and "I" (RCP channel) respectively, on the corresponding observation plane at f=16.7 GHz. The simulation results show good agreement with the design outcomes, demonstrating the feasibility of the proposed method. Figure 7(g, h) display the measurement results under LCP and RCP illumination on the imaging plane, respectively. It can be observed that the measurement results successfully reconstruct the pre-designed images, consistent with the numerical simulation results. The measured images appear blurrier

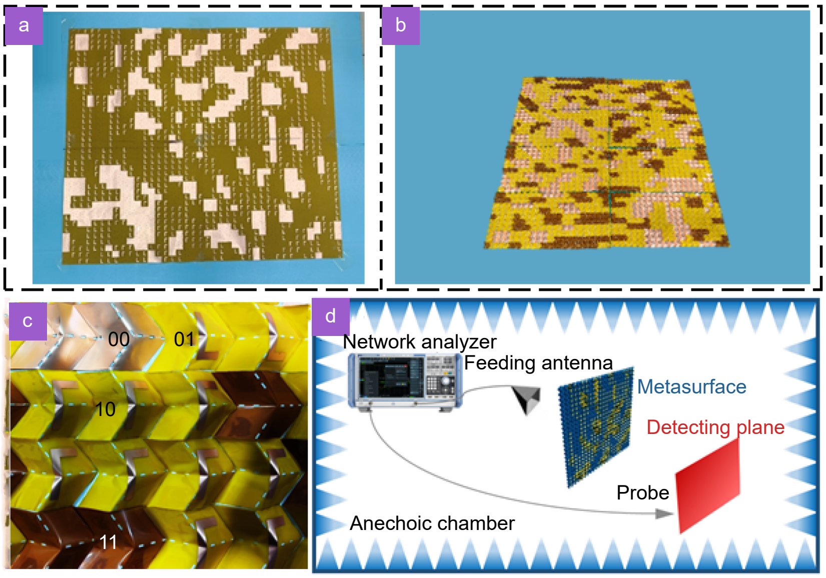

Fig. 6 | The photograph of the (**a**) planar and (**b**) folded (θ=45°) origami metasurface sample. (**c**) In the folded state, the local pattern is represented. '00' denotes pure substrate, '11' denotes pure metal, '01' denotes L-enantiomer, and '10' denotes D-enantiomer. (**d**) Schematic description of the near-field scanning experimental setup.

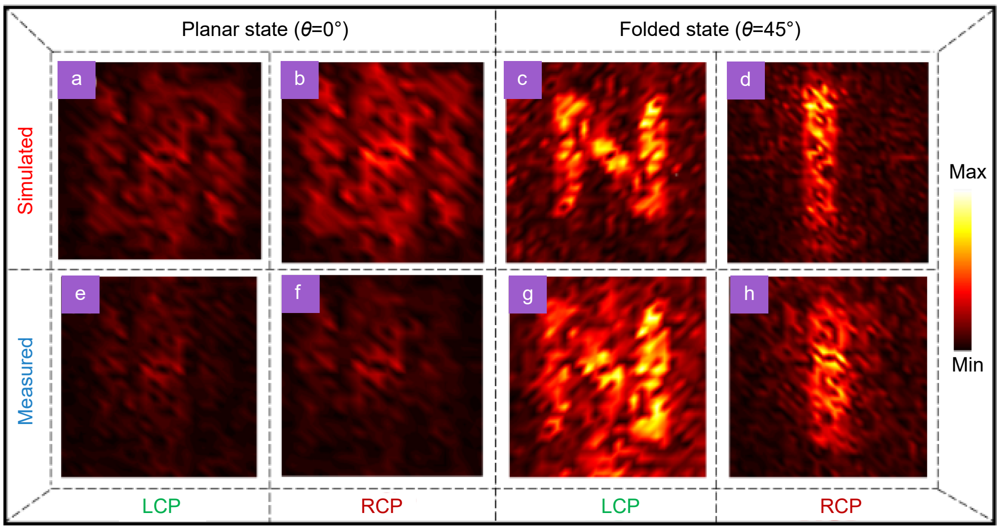

Fig. 7 | Simulation and measurement results. Planar state (*θ*=0°): Simulated results under (**a**) LCP and (**b**) RCP illumination; measured results under (**e**) LCP and (**f**) RCP illumination. Folded state (*θ*=45°): Simulated results under (**c**) LCP and (**d**) RCP illumination; measured results under (**g**) LCP and (**h**) RCP illumination.

than the simulated ones, which is attributed to the manufacturing tolerances of the origami metasurface. Overall, the experimental results show that the imaging mode efficiencies for the "N" and "I" images are 41.79% and 55.20% respectively (with energy concentrated in the image region referring to the total energy on the measured plane), and the peak signal-to-noise ratios (SNRs, defined as the peak intensity in the image divided by the standard deviation of the background noise) are 7.63 and 9.52, respectively. Here, the energy concentrated in the image region, with reference to the total energy on the measured plane, quantitatively describes the contrast between the target pattern and the background. The proposed framework based on Miura-ori origami offers an additional degree of freedom to manipulate CD effects by transforming planar metallic structures into 3D metallic structures through manual mechanical stimulation. With the advancement of 3D printing technology, the functional design of metasurfaces based on Miura-ori origami will become more robust, providing additional avenues for information storage, encryption, and communication applications.

Conclusion

In summary, we propose a paradigm for achieving reconfigurable chiral responses based on Miura-ori origami. In the folded state, the origami chiral structure exhibits pronounced CD, whereas in the planar state, the chiral response vanishes. By switching the folding state of the origami, the functionalities of holographic imaging and encryption can be toggled. Furthermore, based on the Rosenfeld criterion, the physical mechanism of chiral resonance achieved by L-/D-enantiomers is explored through the analysis of surface current distributions. As a proof of principle, in the folded state, holographic images of "N" and "I" are reconstructed under LCP and RCP illuminations, respectively. Both numerical simulations and experimental verifications are conducted for a 40 × 40 pixel prototype. In the planar state, valuable information cannot be extracted from the holographic imaging, realizing holographic encryption. Good agreement between simulation and experimental results demonstrates the feasibility of the proposed scheme. In line with the urgent demands of modern camouflage systems, this scheme can be applied to vital equipment to achieve EM functionalities such as preset information encryption and stealth. As mechanical deformation does not require additional phase-change materials or active lumped elements, origami-based holographic imaging emerges as one of the alternative approaches for EM manipulation, offering an ingenious method to enhance information security levels.

References

1. Sun SL, Yang KY, Wang CM et al. High-efficiency broadband anomalous reflection by gradient meta-surfaces. *Nano Lett* **12**, 6223–6229 (2012).

2. Liu XY, Chen MK, Chu CH et al. Underwater binocular metalens. *ACS Photonics* **10**, 2382–2389 (2023).
3. Yu SX, Li L, Shi GM et al. Generating multiple orbital angular momentum vortex beams using a metasurface in radio frequency domain. *Appl Phys Lett* **108**, 241901 (2016).
4. Chen MK, Liu XY, Wu YF et al. A meta-device for intelligent depth perception. *Adv Mater* **35**, 2107465 (2023).
5. Nan T, Zhao H, Guo JY et al. Generation of structured light beams with polarization variation along arbitrary spatial trajectories using tri-layer metasurfaces. *Opto-Electron Sci* **3**, 230052 (2024).
6. Landy NI, Sajuyigbe S, Mock JJ et al. Perfect metamaterial absorber. *Phys Rev Lett* **100**, 207402 (2008).
7. Yifat Y, Eitan M, Iluz Z et al. Highly efficient and broadband wide-angle holography using patch-dipole nanoantenna reflectarrays. *Nano Lett* **14**, 2485–2490 (2014).
8. Huang K, Dong ZG, Mei ST et al. Silicon multi-meta-holograms for the broadband visible light. *Laser Photonics Rev* **10**, 500–509 (2016).
9. Zhou HQ, Wang YT, Li XW et al. Switchable active phase modulation and holography encryption based on hybrid metasurfaces. *Nanophotonics* **9**, 905–912 (2020).
10. Ding XM, Wang ZC, Hu GW et al. Metasurface holographic image projection based on mathematical properties of Fourier transform. *PhotoniX* **1**, 16 (2020).
11. Naveed MA, Ansari MA, Kim I et al. Optical spin-symmetry breaking for high-efficiency directional helicity-multiplexed metaholograms. *Microsyst Nanoeng* **7**, 5 (2021).
12. Gao H, Fan XH, Wang YX et al. Multi-foci metalens for spectra and polarization ellipticity recognition and reconstruction. *Opto-Electron Sci* **2**, 220026 (2023).
13. Kim J, Jeon D, Seong J et al. Photonic encryption platform *via* dual-band vectorial metaholograms in the ultraviolet and visible. *ACS Nano* **16**, 3546–3553 (2022).
14. Kang D, Heo H, Yang Y et al. Liquid crystal-integrated metasurfaces for an active photonic platform. *Opto-Electron Adv* **7**, 230216 (2024).
15. Li X, Chen LW, Li Y et al. Multicolor 3D meta-holography by broadband plasmonic modulation. *Sci Adv* **2**, e1601102 (2016).
16. Zhang F, Guo YH, Pu MB et al. Meta-optics empowered vector visual cryptography for high security and rapid decryption. *Nat Commun* **14**, 1946 (2023).
17. Liu YC, Xu K, Fan XH et al. Dynamic interactive bitwise metaholography with ultra-high computational and display frame rates. *Opto-Electron Adv* **7**, 230108 (2024).
18. Bao L, Ma Q, Wu RY et al. Programmable reflection–transmission shared-aperture metasurface for real-time control of electromagnetic waves in full space. *Adv Sci* **8**, 2100149 (2021).
19. Zhang XG, Yu Q, Jiang WX et al. Polarization-controlled dual-programmable metasurfaces. *Adv Sci* **7**, 1903382 (2020).
20. Lepeshov S, Krasnok A. Tunable phase-change metasurfaces. *Nat Nanotechnol* **16**, 615–616 (2021).
21. Ding CC, Rui GH, Gu B et al. Phase-change metasurface with tunable and switchable circular dichroism. *Opt Lett* **46**, 2525–2528 (2021).
22. Dong YB, Luan HT, Lin DJ et al. Laser-induced graphene hologram reconfiguration for countersurveillance multisecret sharing. *Laser Photonics Rev* **17**, 2200805 (2023).
23. Chen T, Bilal OR, Lang R et al. Autonomous deployment of a solar panel using elastic origami and distributed shape-memory-polymer actuators. *Phys Rev Appl* **11**, 064069 (2019).
24. Schenk M, Viquerat AD, Seffen KA et al. Review of inflatable booms for deployable space structures: packing and rigidization. *J Spacecr Rockets* **51**, 762–778 (2014).
25. Silverberg JL, Evans AA, Mcleod L et al. Using origami design principles to fold reprogrammable mechanical metamaterials. *Science* **345**, 647–650 (2014).
26. Overvelde JTB, De Jong TA, Shevchenko Y et al. A three-dimensional actuated origami-inspired transformable metamaterial with multiple degrees of freedom. *Nat Commun* **7**, 10929 (2016).
27. Filipov ET, Tachi T, Paulino GH. Origami tubes assembled into stiff, yet reconfigurable structures and metamaterials. *Proc Natl Acad Sci USA* **112**, 12321–12326 (2015).
28. Lin ZW, Novelino LS, Wei HM et al. Folding at the microscale: enabling multifunctional 3D origami-architected metamaterials. *Small* **16**, 2002229 (2020).
29. Zhai ZR, Wu LL, Jiang HQ. Mechanical metamaterials based on origami and kirigami. *Appl Phys Rev* **8**, 041319 (2021).
30. Kuribayashi K, Tsuchiya K, You Z et al. Self-deployable origami stent grafts as a biomedical application of Ni-rich TiNi shape memory alloy foil. *Mater Sci Eng A* **419**, 131–137 (2006).
31. Cheng Q, Song ZM, Ma T et al. Folding paper-based lithium-ion batteries for higher areal energy densities. *Nano Lett* **13**, 4969–4974 (2013).
32. Pesenti M, Masera G, Fiorito F. Exploration of adaptive origami shading concepts through integrated dynamic simulations. *J Archit Eng* **24**, 04018022 (2018).
33. Wang ZJ, Jing LQ, Yao K et al. Origami-based reconfigurable metamaterials for tunable chirality. *Adv Mater* **29**, 1700412 (2017).
34. Li M, Shen L, Jing LQ et al. Origami metawall: mechanically controlled absorption and deflection of light. *Adv Sci* **6**, 1901434 (2019).
35. Zhu ZB, Wang H, Li YF et al. Origami-based metamaterials for dynamic control of wide-angle absorption in a reconfigurable manner. *IEEE Trans Antennas Propag* **70**, 4558–4568 (2022).
36. Zhu ZB, Li YF, Qin Z et al. Miura origami based reconfigurable polarization converter for multifunctional control of electromagnetic waves. *Photonics Res* **12**, 581–586 (2024).
37. Pan RH, Liu Z, Zhu W et al. Asymmetrical chirality in 3D bended metasurface. *Adv Funct Mater* **31**, 2100689 (2021).
38. Liu K, Tachi T, Paulino GH. Invariant and smooth limit of discrete geometry folded from bistable origami leading to multistable metasurfaces. *Nat Commun* **10**, 4238 (2019).
39. Yang SY, Liu Z, Yang HF et al. Intrinsic chirality and multispectral spin-selective transmission in folded eta-shaped metamaterials. *Adv Opt Mater* **8**, 1901448 (2020).
40. Frank B, Yin XH, Schäferling M et al. Large-area 3D chiral plasmonic structures. *ACS Nano* **7**, 6321–6329 (2013).
41. Zheng YL, Chen K, Yang WX et al. Kirigami reconfigurable gradient metasurface. *Adv Funct Mater* **32**, 2107699 (2022).

42. Yin XH, Schäferling M, Metzger B et al. Interpreting chiral nanophotonic spectra: the plasmonic born–Kuhn model. *Nano Lett* **13**, 6238–6243 (2013).
43. Chen Y, Yang XD, Gao J. Spin-controlled wavefront shaping with plasmonic chiral geometric metasurfaces. *Light Sci Appl* **7**, 84 (2018).
44. Kim J, Yang Y, Badloe T et al. Geometric and physical configurations of meta-atoms for advanced metasurface holography. *InfoMat* **3**, 739–754 (2021).
45. Yang SY, Liu Z, Hu S et al. Spin-selective transmission in chiral folded metasurfaces. *Nano Lett* **19**, 3432–3439 (2019).
46. Li BH, Li XW, Zhao RZ et al. Polarization multiplexing terahertz metasurfaces through spatial femtosecond laser-shaping fabrication. *Adv Opt Mater* **8**, 2000136 (2020).

Acknowledgements

We are grateful for financial supports from National Key Research and Development Program of China (No. 2022YFB3806200).

Competing interests

The authors declare no competing financial interests.